

Design of a fluorinated magneto-responsive material with tuneable ultrasound scattering properties†

Cite this: DOI: 10.1039/c3tb21585g

Kévin Zimny,^{‡,ab} Benoit Mascaro,^{‡,c} Thomas Brunet,^c Olivier Poncelet,^c
Christophe Aristégui,^c Jacques Leng,^d Olivier Sandre^{*b} and Olivier Mondain-Monval^{*a}

In this work, we describe the preparation of emulsions of fluorinated ferrofluid droplets suspended in a yield-stress hydrogel (Bingham fluid) with potential applications for ultrasound (US) spectroscopy and imaging. Fluorinated ferrofluids were obtained using an original multi-step process leading to an appropriate suspension of magnetic nanoparticles (MNPs) coated by a layer of fluoroalkylsilane in fluorinated oil. The efficiency of the sol–gel coating reaction was assessed by several methods including infrared and X-ray photoelectron spectroscopy, small angle neutron scattering and magnetometry. The resulting suspension of silanized-MNPs behaves as a true fluorinated ferrofluid, remaining stable (*i.e.* a monophasic suspension of well dispersed MNPs) in magnetic inductions as high as 7 T. These ferrofluids were employed to prepare monodisperse emulsions in a Bingham gel using a robotic injection device. Using ultrasound spectroscopy, we show that the emulsion droplets behave as Mie-type acoustic wave resonators due to the high sound–speed contrast between the droplets and the matrix. When subjected to a magnetic field, the ferrofluid droplets elongate in the field direction, which in return modifies the acoustic response of the material. The resonance frequency peaks scale as the inverse of the emulsion droplet size encountered by the wave propagation vector. These results might open a new road towards the realisation of ultrasound contrast agents guided by magnetic fields and with a tuneable attenuation spectrum.

Received 9th November 2013
Accepted 24th December 2013

DOI: 10.1039/c3tb21585g

www.rsc.org/MaterialsB

1 Introduction

Possessing numerous original properties, fluorinated materials are used in a wide variety of applications such as coating agents for cooking devices or fabrics, as ion exchange membranes or as biomaterials for cardiovascular implants.¹ They present low thermal conductivity, high mass density, chemical inertia, and inflammability. Thus, several companies developed low viscosity perfluoro- or semi-fluorinated oils with good

biocompatibility for applications such as blood substitutes, medical devices or ultrasound contrast agents, together with low environmental cost *i.e.* zero ozone-depletion and a low greenhouse effect of their vapour in the atmosphere.² Toxicological studies were motivated by the spread of perfluoroalkanes in the environment by industry. If perfluorooctanoic acid (PFOA) was shown to exhibit very slow clearance from living organisms,^{3,4} as ascribed to the outstanding stability of carbon–fluorine bonds, other fluorinated chemicals are considered as “bio-safe”. Among them, fluorinated ultrasound contrast agents (UCA) commonly referred to as “microbubbles” are authorized for intravenous injection in humans under brand names such as SonoVue®, Optison®, Imavis®, Definity®, Imagent®, *etc.*

Due to their very low solubility in water (less than 10 ppm) and, in contrast, to their high compressibility and ability to dissolve large quantities of gases (O₂, N₂, CO₂, *etc.*),⁵ volatile fluorocarbons can indeed be used to fill the inner components of microbubbles. The UCA echogenicity relies on the impedance contrast between tissues mainly made of water ($Z_{\text{water}} \approx 1.5 \times 10^6$ Rayl) and the materials to be injected, which is often a gas phase ($Z_{\text{air}} \approx 340$ Rayl). However, gas microbubbles also have a short lifetime due to their physicochemical instability in a fluid and tendency to rapidly burst or to coalesce. One way to increase the lifetime of UCA in blood is by mixing air with a

^aUniversité de Bordeaux, CRPP/CNRS UPR 8641 Centre de Recherche Paul Pascal, 115 avenue Schweitzer, 33600 Pessac, France. E-mail: mondain@crpp-bordeaux.cnrs.fr

^bUniversité de Bordeaux, LCPO/CNRS UMR 5629 Laboratoire de Chimie des Polymères Organiques, 16 avenue Pey Berland, 33607 Pessac, France. E-mail: olivier.sandre@enscbp.fr

^cUniversité de Bordeaux, I2M-APY/CNRS UMR 5295 Institut de Mécanique et d'Ingénierie, 351 cours de la libération, 33405 Talence, France

^dUniversité de Bordeaux, LOF/Solvay/CNRS UMR 5258 Laboratory of Future, 178 avenue Schweitzer, 33600 Pessac, France

† Electronic supplementary information (ESI) available: Complete XPS spectra and movies of the deformation of a single fluorinated ferrofluid droplet embedded in a water-based gel matrix submitted to the magnetic field created (1) by a permanent magnet; and (2) by a solenoid producing an increasing magnetic induction between $B = 0$ and $B = 46$ mT. See DOI: 10.1039/c3tb21585g

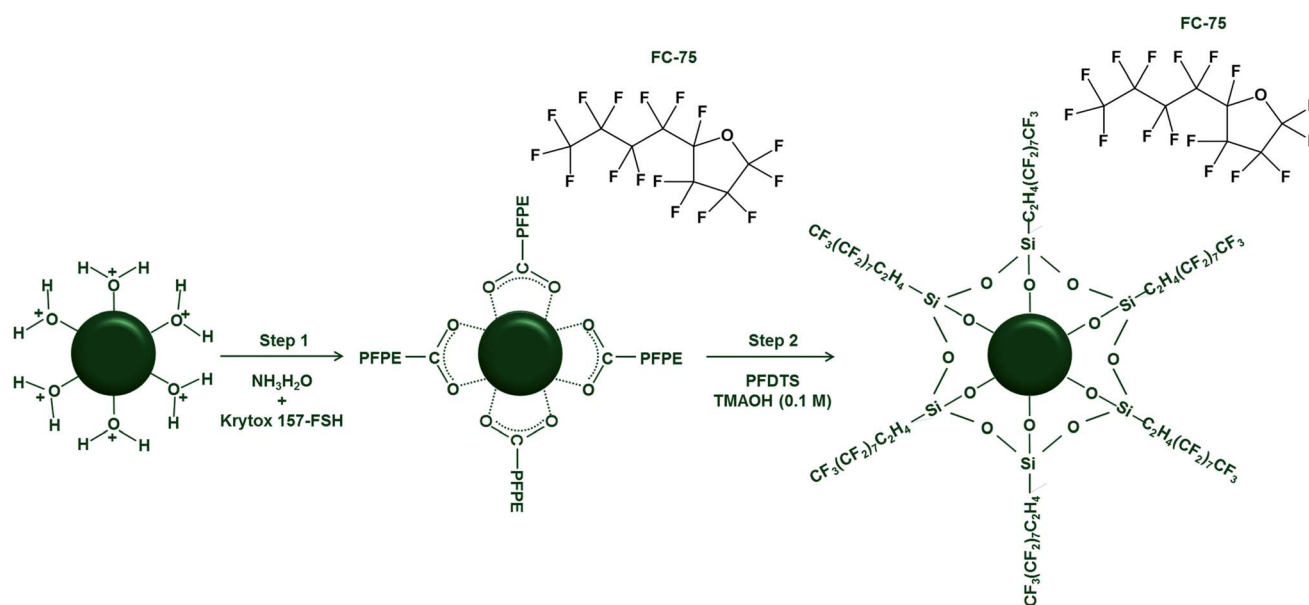
‡ These authors contributed equally.

perfluorocarbon gas that presents very low solubility in water, thus acting as “osmotic agents” and slowing down the Ostwald ripening process.⁵ Several routes were developed to obtain longer-lasting UCA, on the one hand by coating the bubbles with a stabilising shell of lipids or polymers^{6,7} and on the other hand by adding to air or nitrogen a partial pressure of fluorinated gas, in that case wrapped by a shell of hydrogenated⁸ or F-alkylated double-tailed phospholipids.⁹ Typical volatile fluoroalkanes incorporated into microbubbles are octafluoropropane,¹⁰ decafluorobutane,¹¹ tetradecafluorohexane (commercialised by 3M as the Fluorinert™ FC-72 reference),^{8,9} or perfluorooctylbromide (PFOB).⁷ Recently, several teams reported the decoration of the surface of microbubbles by iron oxide nanoparticles, both for pure air¹² and for mixed air/fluorocarbon gas bubbles.^{10,13} The idea was to be able to guide such magnetic microbubbles against the strong flow-rate of blood circulation by the use of a magnetic field gradient.

Thus, the US imaging community is still in search for alternatives to gas bubbles, which present a high echogenicity but poor long term stability. We propose here a new type of material made of fluorinated ferrofluid oil droplets exhibiting both a large sound-speed contrast ($\sim 1/3$) with aqueous media ($500 \text{ m s}^{-1}/1500 \text{ m s}^{-1}$) and sensitivity to an external magnetic fluid. When dispersed in an aqueous yield-stress matrix, magnetic fluorinated oil droplets are not only magnetically guidable but also exhibit strong Mie resonances at specific frequencies,¹⁴ varying with the intensity of an applied magnetic field and its orientation with respect to the wave propagation vector. Such magneto-responsive attenuation properties are described precisely in a companion article.¹⁵ The present manuscript deals with chemistry and soft-matter methods necessary to

build this tuneable acoustic material. First, we describe the process used to synthesise the magnetic nanoparticles and to coat them with a layer of perfluorosilane. This fluorinated ferrofluid is then fully characterised by using different spectroscopic, microscopic and magnetic methods. Finally, we present the fabrication of a monodisperse emulsion in an aqueous yield-stress fluid and an example of tuneable acoustic properties.

Since decades, sol-gel methods have opened a golden gate towards the so-called “soft chemistry” which enables to obtain organic-inorganic nano-sized or nano-structured hybrid materials based on silica exhibiting a wide variety of structures and morphologies, and more recently on metal-oxide frameworks.¹⁶ Organosilanes are commonly used to functionalise silica surfaces by a hydrolysis-condensation mechanism initiated at the inorganic surface, which is rich in silanol moieties (Si-OH) arising from the hydrated state of the solid surface. Monolayers of semi-fluorinated alkylsilanes are chosen for instance to render glass surfaces highly hydrophobic.^{17,18} The same reactions exist for the hydrated surface of iron oxide (Fe-OH groups), but they have been much less developed. The chemical grafting of molecules onto iron oxides often starts by coating with a molecular monolayer of (3-aminopropyl)triethoxysilane (APTS).¹⁹⁻²⁷ This short molecule is too small to bring enough electrosteric repulsions between particles to confer any colloidal stability to the MNPs in water, but they provide amino groups enabling further functionalisation steps. Several studies involve a ligand-exchange process starting from an initial oleic acid monolayer that is replaced by organosilane.^{26,28-30} Apart from APTS, other organosilanes were grafted onto the surface of iron oxide MNPs such as (3-glycidyloxypropyl)trimethoxysilane,³¹



Scheme 1 Fluorinated ferrofluid preparation in two steps. The proper dispersion of iron oxide nanoparticles in a fluorinated oil involves: step 1: adsorption of a perfluoropoly(ether) surfactant (Krytox™ 157-FSH) onto the nanoparticles and phase transfer into a fluorinated oil such as perfluoro-2-butyltetrahydrofuran (Fluorinert™ FC-75); step 2: ligand exchange, and then chemical grafting (sol-gel reaction) of 1H,1H,2H,2H-perfluorodecyltriethoxysilane (PFDTs) directly onto the hydroxyl groups of the iron oxide surface. The two steps were performed in alkaline media (respectively ammonium hydroxide and tetramethylammonium hydroxide).

cianoethyltrimethoxysilane,³² or 2-bromo-2-methyl-*N*-(3-(triethoxysilyl)propyl)propanamide to initiate the polymer chain growth by a “grafting-from” controlled polymerisation method.³³ In almost all the previous studies, silanization was an intermediate step needed to anchor a molecular shell around the magnetic cores by covalent bonds, which is preferable compared to the most common adsorption routes with chelating ligands such as carboxylic acids, phosphates, sulfonates or catechols. Only macromolecular silanes such as triethoxy(methoxypolyethyleneoxy)silane²⁹ or trifluoroethylsterpoly(ethylene glycol)³⁰ were shown to achieve direct colloidal stabilisation of MNPs in water before any further coupling reaction.

Approach developed here

In this study, we propose to accomplish the chemical grafting of 1*H*,1*H*,2*H*,2*H*-perfluorodecyltriethoxysilane (PFDTs) leading to stable colloidal suspensions of iron oxide MNPs in fluorinated oils. The goal of this magnetic fluid is to remain monophasic whatever the strength of an applied magnetic field, which is the definition of a fluorinated “true ferrofluid” (as opposed to a magneto-rheological fluid, where the MNPs make dipolar chains under a magnetic field). Due to the insolubility of perfluorinated molecules in hydrogenated solvents, we propose a route (Scheme 1) starting from the adsorption of perfluoropoly(ether)carboxylic acid (PFPE-COOH, Krytox™ 157-FSH, Dupont) onto the positively charged surface of iron oxide followed by ligand-exchange and silanization with PFDTs, leading to stable fluorinated ferrofluids.

2 Experimental section

Preparation of a fluorinated ferrofluid

Synthesis of magnetic iron oxide nanoparticles. Magnetic nanoparticles (MNPs) were prepared by coprecipitation of iron^{II+} and iron^{III+} salts in alkaline media followed by surface charge reversal in nitric acid and oxidation with iron nitrate according to the Massart procedure.³⁴ At first, 180 g of FeCl₂·4H₂O were mixed with 100 mL of HCl (37%) and 500 mL of deionised water. The mixture was stirred until complete dissolution of FeCl₂. After addition of 365 mL of FeCl₃ (45%) and 2 L of deionized water, 1 L of ammonia solution (28%) was added rapidly under vigorous stirring (800 rpm). The obtained magnetite particles were then collected after sedimentation on a strong magnet. After washing the precipitate with water, 360 mL of nitric acid and 2 L of water were added. Then, 323 g of Fe(NO₃)₃·9H₂O was added to 800 mL of water in order to oxidise the magnetite particles (Fe₃O₄) to maghemite (γ-Fe₂O₃). After sedimentation and washing, the addition of water leads to the formation of a stable aqueous ferrofluid. The obtained magnetic nanoparticles are dispersed in water due to their positive surface charge under acidic conditions. The synthesised nanoparticles were separated into two fractions of hydrodynamic sizes, respectively $D_H = 11$ nm (PDI = 0.013) and $D_H = 36$ nm (PDI = 0.024) following a size-sorting procedure based on the phase-separation by the addition of the electrolyte

in excess to screen electrostatic repulsions.³⁵ The smaller size fraction (SP aqueous ferrofluid) was used mainly for the study of the fluorinated coating, while the larger size fraction (LP aqueous ferrofluid) enabled preparation of magnetic emulsions in water-based gels with larger magnetic susceptibility and thus higher deformations of the drops for a given magnetic field.

Fluorinated surfactant coating

At first, the MNPs were coated with a high molecular weight (7500 g mol⁻¹ nominal, ~5000–6000 g mol⁻¹ measured³⁶) perfluoropoly(ether) end-functionalised with a carboxylic acid group (PFPE-COOH, Krytox™ 157-FSH, Dupont), which enables transferring them from water to perfluoro-2-butyltetrahydrofuran (Fluorinert™ FC-75, 3M) (see step 1 in Scheme 1). Krytox™ 157-FSH was first mixed with ammonium hydroxide to form a carboxylate salt. The aqueous ferrofluid was afterwards directly added to this mixture (molar ratio $n(\gamma\text{-Fe}_2\text{O}_3)/n(\text{PFPE}) = 30$). Under such conditions, the deprotonated carboxylic head-groups of Krytox™ molecules bear a negative charge and adsorb onto the positively charged iron oxide surface. The obtained system was then washed several times with acetone in order to separate the Krytox™-covered MNPs from the polar mixture. Then, ethanol was added and the precipitate was collected after sedimentation on a strong permanent magnet. After three steps of washing with ethanol and acetone, fluorinated oil FC-75 was added to achieve a suspension around 4 wt% and the residual solvents were eliminated by heating 1 hour at 353 K in an oven. After this drying step, the ferrofluid is referred to as the “surfactant ferrofluid”. These surfactant-ferrofluids present a high viscosity (>0.1 Pa s) incompatible with deposition through capillaries. This high viscosity is due to the relatively high viscosity of the FC75/Krytox™ continuous phase. In addition, the interfacial tension γ between the ferrofluid and a dilute Carbopol™ solution ($\gamma = 25$ mN m⁻¹ as measured using a pendant drop experiment on a pendant and sessile drop tensiometer Krüss™ DSA100) seems too high to observe deformation of the droplets under a magnetic field of reasonable intensity (*i.e.* of induction B less than 60 mT).

Ligand exchange and silanization

A second step of ligand exchange was performed in order to replace Krytox™ 157-FSH surfactants by organofluorosilanes, with the purpose of grafting them covalently onto the MNPs (step 2 in Scheme 1). The chosen fluoroalkylsilane, 1*H*,1*H*,2*H*,2*H*-perfluorodecyltriethoxy-silane (PFDTs, Sigma-Aldrich), was added in large excess ($n(\text{PFDTs})/n(\text{PFPE}) = 12$) directly to the surfactant-based ferrofluid in FC-75 (or another oil from the Fluorinert™ series such as the less volatile FC-40). It was first hydrolysed and then condensed around the MNPs *via* a sol-gel process. The reaction occurred under basic conditions with tetramethylammonium hydroxide (TMAOH, Sigma, 0.1 M) as a catalyst. The mixture was placed under stirring (300 rpm) for 3 days at 343 K. The sample was washed several times with water, ethanol and acetone then isolated on a magnet in order to remove the unreacted silane. MNPs were

finally dried in a vacuum oven for 1 hour at 353 K and afterward dispersed in fluorinated oil FC-75 at a concentration of 300 g L⁻¹, representing the volume and weight fractions of 6 vol% (15 wt%) of iron oxide according to the mass densities (respectively 5 g cm⁻³ for γ -Fe₂O₃ and 1.77 g cm⁻³ for the fluorinated oil FC-75). After this second step, the ferrofluid referred to as the “silanized ferrofluid” presents low values of viscosity and interfacial tension with a dilute solution of Carbopol™ in water ($\gamma = 11$ mN m⁻¹ as measured by a pendant drop experiment).

Preparation of the monodisperse magnetic emulsion

Aqueous gel. A yield-stress (Bingham) fluid was prepared by mixing 0.5 g of ramified sodium poly(acrylate) (Carbopol™ 2050 ETG) with 100 mL of deionised water at 323 K. After 30 minutes of stirring at 170 rpm, the mixture was aged at room temperature for 40 min. Finally, 0.5 mL of NaOH at 10 M was added under vigorous stirring until the pH reached 7 ± 0.5 . The gel was then diluted with deionised water to obtain a range of concentration comprised between 0.05% and 0.5% w/w then centrifuged at 6000 rpm in order to remove bubbles. Rheological measurements were performed on an AR2000 TA Instruments rheometer to determine the yield stress at different concentrations. The magnetic emulsions described in this paper were prepared in Carbopol™ gels at 0.05% w/w. In this case, the rheological curve exhibits a yield stress of 1.5 Pa.

Injection of the ferrofluid into the gel to prepare the emulsion

Using robotics, the fluorinated ferrofluids were injected through silica capillaries (coated by polyimide) directly into the aqueous gel. Silica capillaries with a respective internal diameter (ID)/outer diameter (OD) of 40/105 μ m and 75/150 μ m purchased from Polymicro™ Technologies were inserted in the corresponding sleeves of OD = 1/16" (respectively F-237 and F-238, Upchurch™). The sleeve was inserted in a 10–32 PEEK nut with a 1/16" OD ferrule (Upchurch™) connected through a P-659 Luer-lock to a syringe. As previously done for bubbly media³⁷ or fluorinated oil droplets,^{14,38} periodic rows of regularly spaced fluorinated ferrofluid droplets were deposited by a motorised motion of the capillary relatively to the gel. The magnetic fluorinated oil was continuously pushed into the aqueous gel by a 0–1.8 bar pressure generator (Elveflow™ AF1, Elvsys®, Paris, France). Motorised displacements of the plate led to the formation of aligned droplets. Samples made of series of drop lines suspended in the hydrogel were then transferred into the measurement cell ($4 \times 4 \times 3$ cm³) placed inside an electromagnet made of two solenoids (1000 turns each) connected in series with a U-shape soft iron polar piece and an air gap of 4 cm. The magnetic induction B was measured using a LakeShore™ 425 Hall-probe gaussmeter.

Analytical methods

Transmission electron microscopy (TEM). Transmission electron microscopy micrographs were recorded on a Hitachi H7650 microscope working at 80 kV. Samples were diluted at ~ 0.2 g L⁻¹ in the volatile perfluorohexane (Fluorinert™ FC-72)

and sprayed onto the grids. The images were analysed by automated particle counting after threshold and watershed filters using the ImageJ software (<http://rsbweb.nih.gov/ij/>).

Attenuated total reflection infrared (ATR IR) spectroscopy

Infrared measurements were performed on a Bruker Tensor 27 FT-IR spectrometer using the Diamond attenuated total reflection method. Samples were analysed after drying for 1 h in a vacuum oven at 353 K. The IR spectra were recorded in the wave number range 800–4000 cm⁻¹.

X-ray photoelectron spectroscopy (XPS)

A VG Scientific 220 i-XL ESCALAB spectrometer was used for the MNP surface analysis (at a maximal depth of 10 nm) with a non-monochromatised MgK α source ($h\nu = 1253.6$ eV) at 130 W (13 kV and 10 mA). A pressure of 10⁻⁷ Pa was maintained in the chamber during analysis. The analysed area was about 150 μ m in diameter. The full spectra (0–1150 eV) were obtained with a constant pass energy of 150 eV and high resolution spectra at a constant pass energy of 40 eV. Charge neutralisation was required for all insulating samples. The peaks were referenced to Si_{2p} maximum shifted at 103.5 (± 0.1) eV. High resolution spectra were fitted and quantified using the AVANTAGE software provided by ThermoFisher Scientific.

Dynamic light scattering (DLS)

DLS measurements were performed using a nanoparticle size analyser Vasco™ DL135 (Cordouan Technologies, Pessac, France) equipped with a diode laser operating at a 650 nm wavelength at 30% of full power, and a photodiode detector collecting backscattered light at an angle of 135°. For each sample, intensity measurements were carried out at 298 K in a multi-acquisition mode implying 20 correlograms. The Z -average diameters and polydispersity indexes (PDI) of the nanoparticles were obtained by fitting each correlogram with the 2nd order Cumulant algorithm. The time interval and number of channels were fixed for each measurement at 11 and 1000 μ s respectively. The size distribution histograms were generated after each acquisition using the Pade–Laplace inversion algorithm. After accumulation of 20 curves, the obtained histograms were fitted with a log-normal function. Hydrodynamic size histograms obtained by the Cumulants and Pade–Laplace analyses were compared.

Volume fraction measurements

At first, MNPs were diluted, either in dilute HNO₃ (at pH 2) for aqueous ferrofluids or fluorinated oils for the fluorinated ferrofluids (FC-40 or FC-75). They were then analysed by UV-Vis. UV-Vis spectra were recorded in quartz cuvettes on a Molecular devices spectrophotometer SpectraMax™ between 240 and 800 nm by a step of 4 nm. The molar concentrations were determined by fitting a calibration curve^{39,40} and converted into volume fractions using the tabulated mass densities. Another method based on direct mass density measurement was employed for highly concentrated suspensions for which the

volume was impossible to control with a micropipette. In that case, plastic tubing of a given length and diameter was simply weighed using a precision balance in order to determine the mass density. Then, the MNP volume fraction ϕ was computed from the apparent mass density $\rho = \phi\rho_{\text{iron oxide}} + (1 - \phi)\rho_{\text{FC-75}}$ where $\rho_{\text{iron oxide}} = 5 \text{ g cm}^{-3}$ and $\rho_{\text{FC-75}} = 1.77 \text{ g cm}^{-3}$ are the mass densities of iron oxide and FC-75 oil, respectively.

Small angle neutron scattering (SANS)

SANS curves were recorded on the PACE spectrometer at the LLB-CEA Saclay neutron facility, France. The scattering wave vector q ranged from 0.00243 \AA^{-1} to 0.37 \AA^{-1} thanks to the use of 3 different configurations: “small- q range” (sample-to-detector distance $D = 4.7 \text{ m}$, neutron wavelength $\lambda = 17 \text{ \AA}$), “medium- q range” ($D = 3 \text{ m}$ and $\lambda = 6 \text{ \AA}$), and “large- q range” ($D = 1 \text{ m}$ and $\lambda = 6 \text{ \AA}$). The samples analysed in 1 mm thick quartz cuvettes exhibited low incoherent background due to their low hydrogen content. The curves were converted into absolute intensity units (cm^{-1}) using calibration by standards (subtraction using the empty cell and normalisation using the signal of H_2O to take into account the efficiency of the detector).⁴¹ The SANS curves were fitted with a polydisperse core-shell form factor using the SASView program available at <http://www.sasview.org/>. The values of neutron scattering length density (SLD) were calculated using the chemical formulae and tabulated values of the atomic neutron scattering lengths. These SLD values were 6.98, 2.1, and $3.84 \times 10^{10} \text{ cm}^{-2}$ respectively for $\gamma\text{-Fe}_2\text{O}_3$, PFDTs, and FC-75.

Superconducting quantum interference device (SQUID)

Magnetisation curves were recorded at room temperature using a Quantum Design™ MPMSXL SQUID magnetometer from 0 to 7 T. MNPs were diluted at 1% v/v in HNO_3 pH 2 for aqueous ferrofluids or in FC-75 for fluorinated ferrofluids. A wet mass around 1 mg of each sample (including solvent) was weighed precisely in an impermeable bag sealed at the end of a plastic straw inserted inside the magnet hole. The diamagnetic contribution of the solvent was fitted by a negative slope line (dominant at high field) subtracted from the total curve to yield the contribution of the MNPs only.

3 Results and discussion

Sizes and colloidal stability of MNPs in fluorinated oils

The size and colloidal stability in fluorinated oils was assessed by DLS (Table 1). Two kinds of fluorinated nanoparticles were prepared in this work. They were noted ‘surfacted’ after coating with the Krytox™ surfactant (step 1 in Scheme 1) and ‘silanized’ after grafting with the PFDTs silane (step 2 in Scheme 1). Sample 1 was prepared from an aqueous ferrofluid of larger nanoparticles noted ‘aqueous LP’ and used to produce magnetic emulsions in gels whereas Sample 2 was prepared from ‘aqueous SP’ and used for the SANS experiment described further. The different size measurements performed on the two samples at the various steps of the coating procedure are given in Table 1.

Table 1 Hydrodynamic (DLS) and physical (TEM) diameters of the nanoparticles for several prepared ferrofluids

	Cumulants ^a		Pade-Laplace ^b		TEM analysis $\langle D \rangle \pm \Delta D$ (nm)
	Z-Ave (nm)	PDI	$\langle D \rangle$ (nm)	CV (%)	
LP (Sample 1)					
Aqueous	36.5	0.024	35.9	6.9	NM ^c
Surfacted	68	0.07	79.3	135	NM ^c
Silanized	51	0.05	51.5	6.4	9.3 ± 3.4
SP (Sample 2)					
	Cumulants ^a		Pade-Laplace ^b		TEM analysis $\langle D \rangle \pm \Delta D$ (nm)
	Z-ave (nm)	PDI	$\langle D \rangle$ (nm)	CV (%)	
Aqueous	11	0.013	10.1	11.2	NM ^c
Surfacted	91.5	0.09	99.1	79.6	5.8 ± 2.6
Silanized	56.2	0.065	57.3	8.6	7.3 ± 2.3

^a 2nd order cumulant fit (Z-average diameter and polydispersity index).
^b Pade-Laplace fit (mean diameter, coefficient of variation) of the DLS correlograms for aqueous, Krytox™-‘surfacted’ and PFDTs-‘silanized’ ferrofluids. Sample 1 was prepared from the large fraction (aqueous LP). Sample 2 was prepared from the smaller size fraction (aqueous SP).
^c NM: not measured.

The two methods used to analyse the DLS data lead to roughly the same average particle diameters and broadness of the distribution (the values of PDI and CV being clearly correlated). After step 1 (coating with Krytox™), the ‘surfacted’ nanoparticles remain dispersed and stable but exhibit a significant size and size-dispersity increase (Z-average hydrodynamic diameters respectively of 68 and 92 nm for the two batches LP and SP, PDI respectively 0.07 and 0.09). This result indicates that the MNPs tend to aggregate when coated with the fluorinated surfactant Krytox™ 157-FSH. After step 2 (chemical grafting of perfluorinated organosilane onto the particle surface), one observes a decrease of the sizes of MNPs and of the polydispersity index that reveals an improved colloidal stability and a narrower size distribution. The mean diameter of the MNPs and their coefficient of variation (CV), both calculated by fitting the Pade-Laplace histogram with a log-normal distribution law, show the same evolution. The results exhibit a large CV difference between surfacted and grafted ferrofluids. Fig. 1 shows the evolution of the hydrodynamic diameter for three different samples before and after grafting with PFDTs. In all cases, each ‘silanized’ ferrofluid presents a lower hydrodynamic diameter and a sharper distribution than the corresponding ‘surfacted’ ferrofluid.

Transmission electron microscopy (TEM)

The MNPs were also directly imaged by TEM (Fig. 2). The sizes of the MNPs deduced by image analysis of these pictures are given in Table 1.

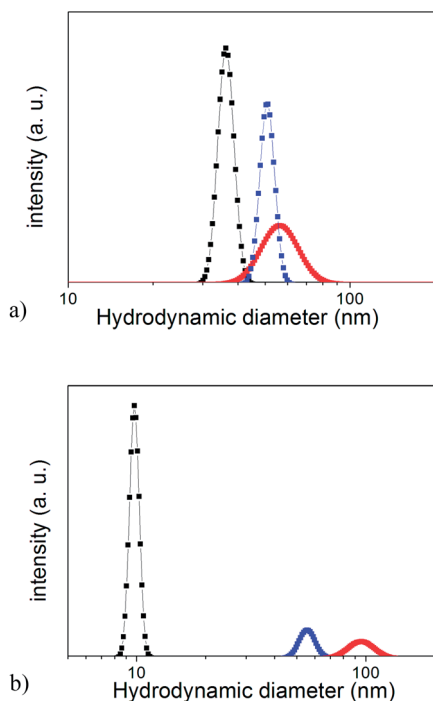


Fig. 1 Evolution of the hydrodynamic diameter at different steps of the synthesis obtained by fitting the Pade–Laplace histograms with log-normal laws. Aqueous (black line), ‘surfacted’ (red line) and ‘silanized’ ferrofluids (blue line) for (a) Sample 1 (LP), and (b) Sample 2 (SP).

The sizes deduced by TEM are much smaller than those deduced by DLS, which indicates that the magnetic cores observed individually on the TEM pictures form clusters of several nanoparticles when suspended in a liquid. To represent the size-dispersity, the histograms of the diameters d obtained by DLS (Fig. 1) or TEM (Fig. 2) were all fitted by a log-normal distribution law of median value d_0 and characteristic broadness σ , as written below.

$$P(d) = \frac{1}{\sqrt{2\pi}\sigma d} \exp\left[-\frac{1}{2\sigma^2}\left(\ln\frac{d}{d_0}\right)^2\right] \quad (1)$$

On a logarithmic scale such as the horizontal axis of Fig. 1, this distribution looks like a Normal law, σ being the standard deviation of $\ln(d)$. Then, the moments of the distribution can be easily calculated. In particular the number-averaged (d_n) and volume-averaged (d_w) diameters are obtained respectively by the following formulae.

$$d_n = \langle d \rangle = d_0 \exp(\sigma^2/2) \quad (2)$$

$$d_w = \langle d^4 \rangle / \langle d^3 \rangle = d_0 \exp(7\sigma^2/2) \quad (3)$$

For example, ‘silanized’ sample 1 (LP) has $d_n^{\text{TEM}} = 10.2$ nm and $d_w^{\text{TEM}} = 19.1$ nm. At larger magnification (Fig. 3), the TEM micrographs evidence the presence of a shell around the nanoparticles, which has a lower electron density than iron oxide. The size of this shell can be estimated at approximately 3 nm for sample 1 (Fig. 3). These observations are consistent with the formation of multi-layers of fluorinated

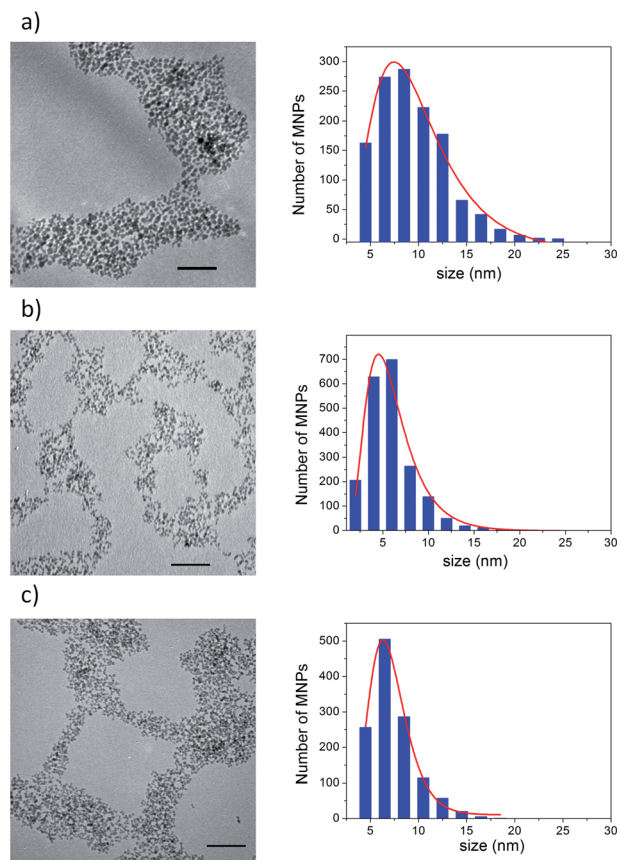


Fig. 2 TEM micrographs and their corresponding size histograms deduced from image analysis and fitted with a log-normal function. (a) ‘Silanized’ sample 1 (LP, 9.3 ± 3.4 nm); (b) ‘surfacted’ sample 2 (SP, 5.8 ± 2.6 nm); (c) ‘silanized’ sample 2 (SP, 7.3 ± 2.3 nm). Scale bars represent 100 nm.

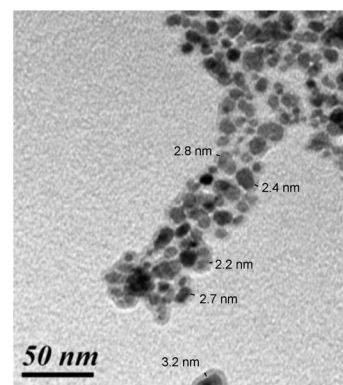


Fig. 3 High resolution TEM micrographs of the ‘silanized’ sample 1 (LP). The scale bar represents 50 nm. The thickness of the silica-rich shell is measured at several locations on this image.

silica around the MNPs. With sample 2 (from the aqueous SP batch), the size of the MNPs goes from around 5.8 nm before grafting to 7.3 nm after grafting. The 1.5 nm difference can be assigned to the formation of a silica shell around the MNPs.

Small angle neutron scattering (SANS)

The effect of different coatings on the colloidal stability of the MNP dispersion in FC-75 oil was further studied by SANS with the nanoparticles of smaller sizes (sample 2). The intensity curve of the PFDTS-silanized MNPs (Fig. 4) was well fitted by the form factor of a polydisperse suspension of core-shell particles modelled by an inorganic core radius $R_0 = 2.34$ nm (log-normal dispersion of standard width $\sigma = 0.33$, SLD of $\gamma\text{-Fe}_2\text{O}_3$) wrapped by a silicon-rich shell of thickness $t_0 = 1.45$ nm (polydispersity $\sigma = 0.64$, SLD of PFDTS) suspended in a medium with the theoretical SLD of the FC-75 oil. Near the lowest scattering vectors q , the Guinier approximation enables the measurement of a radius of gyration $R_G = 5.1$ nm compatible with individually dispersed MNPs. In contrast, the curve for the KrytoxTM-surfaced ferrofluid could not be fitted simply by a core-shell form factor, presumably due to the contribution of cross-particle correlations (structure factor due to attractions). In that case, the Guinier plot leads to a gyration radius $R_G = 29$ nm, attesting the presence of finite sized aggregates of MNPs. From these SANS experiments, we deduce that the grafting of fluoroalkylsilane onto the MNPs greatly improved the quality of the dispersion in the fluorinated oil compared to the mere adsorption of a fluorinated surfactant.

Spectroscopic study of the chemical grafting onto iron oxide

ATR IR spectroscopy. The efficiency of the grafting reaction was assessed by FT-IR spectroscopy. We display the spectra in three different regions ($800\text{--}1400$ cm^{-1} , $1500\text{--}2000$ cm^{-1} , and $2500\text{--}4000$ cm^{-1}) in order to ease the discussion on all the information that can be deduced.

Evidence for the surfactant adsorption at the surface of the MNPs (step 1) can be deduced from the comparison of the spectra of pure KrytoxTM 157-FSH and the KrytoxTM-surfaced ferrofluid (Fig. 5: spectra A and B). The IR spectrum of pure KrytoxTM 157-FSH contains a large band at 980 cm^{-1} (band (a) in Fig. 5) characteristic of the stretching of CF_3 bonds in the

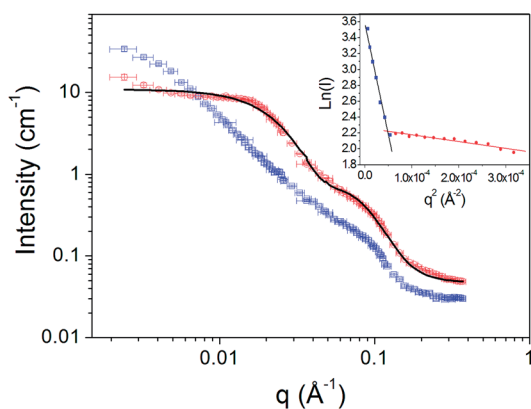


Fig. 4 SANS curves of the KrytoxTM-surfaced ferrofluid (blue markers), PFDTS-silanized MNPs (red markers) and fit by a polydisperse core-shell form factor (solid line). The volume fractions ϕ are respectively 0.5% and 3.4%. Inset: Guinier plots of $\ln(I(q))$ as a function of q^2 enabling to measure the gyration radii R_G from the slope $-R_G^2/3$.

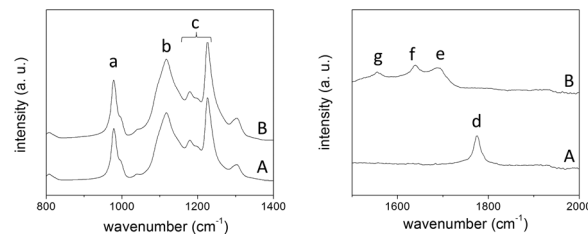


Fig. 5 ATR-IR spectra of KrytoxTM 157-FSH (spectrum A) and KrytoxTM-surfaced MNPs (spectrum B) in two wave number ranges. The letters indicate absorption peaks discussed in the text.

fluoropropylene oxide groups of the perfluoro-poly(ether) backbone.⁴² The broad band at 1117 cm^{-1} is ascribed to C-O stretching mode (b). Absorption bands at 1180 , 1200 and 1230 cm^{-1} correspond to different stretching modes of CF_x groups (c). The band at 1780 cm^{-1} (d) is assigned to carbonyl stretching of carboxylic acid.⁴³ For the KrytoxTM-surfaced ferrofluid, band (d) is replaced after step 1 by three new bands at 1680 (e), 1630 (f) and 1540 cm^{-1} (g) respectively attributed to the ammonium carboxylate salt of KrytoxTM, asymmetric and symmetric COO^- stretching. These bands indicate that the KrytoxTM carboxylate moiety is chemisorbed onto the metal oxide through bidentate chelating interaction.⁴⁴⁻⁴⁶

Now comparing the spectra of PFDTS before and after hydrolysis and condensation (Fig. 6: spectra C and D), the spectrum of unhydrolysed PFDTS silane (D) presents a group of three peaks at 2980 , 2933 and 2892 cm^{-1} (h) that can be attributed to the C-H stretching from the CH_2 and $\text{O-CH}_2\text{-CH}_3$ groups of PFDTS. The broad peak observed at 959 cm^{-1} (i) is characteristic of the Si-OEt bonds. After hydrolysis-condensation (spectrum C), the intensities of bands (h) and (i) decrease strongly, thus confirming the almost total hydrolysis of PFDTS. Indeed, upon hydrolysis, the $\text{O-CH}_2\text{-CH}_3$ groups initially present on the PFDTS molecules are transformed into $\text{CH}_3\text{-CH}_2\text{OH}$ and no longer contribute to the signal of band (h). A new broad band appears at 3340 cm^{-1} (j) corresponding to the O-H stretching mode of H-bonded silanol groups, which shows that condensation is not complete in the bulk system. Spectrum (C) presents three peaks at 1020 , 1070 and 1112 cm^{-1} (k) that can be attributed to the formation of siloxane bonds Si-O-Si.⁴⁷ The other bands observed at 1143 , 1200 and 1230 cm^{-1} (l) are characteristic of the $-\text{CF}_2$ stretching modes.⁴⁸

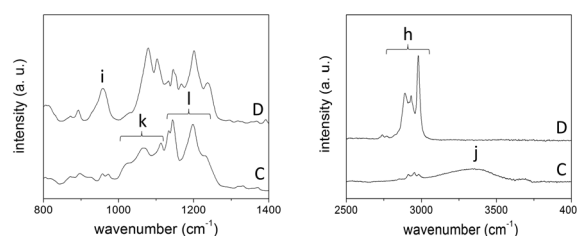


Fig. 6 ATR-IR spectra of hydrolysed and condensed PFDTS (spectrum C) and unhydrolysed PFDTS (spectrum D) in two wave-number ranges. The letters indicate absorption peaks discussed in the text.

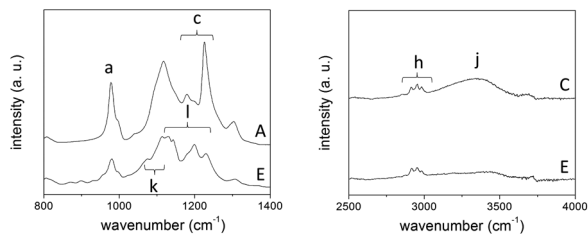


Fig. 7 ATR-IR spectra of Krytox™ 157-FSH (spectrum A), PFDTs powder (spectrum C), and PFDTs-coated MNPs (spectrum E). The letters indicate absorption peaks discussed in text.

Finally, in the spectrum of 'silanized' MNPs (Fig. 7: spectrum E), the almost total disappearance of band (j) observed after grafting onto the MNPs indicates a good condensation of the silica species around the MNPs.⁴⁹ Besides, the bands of CH₂ groups of PFDTs are still detected (h), which indicates the presence of fluorosilane at the MNP surface. Adsorption due to fluorinated chains (l) partially overlaps the band at 1070 cm⁻¹ (k) associated with the formation of the Si–O–Si network. The presence of the bands at 1070 and 1112 cm⁻¹ (k) indicates a high degree of condensation of silica species.⁴⁷ By comparing spectra (A) and (E) (pure Krytox™ vs. 'silanized' MNPs), a strong decrease of the intense band (c) at 1230 cm⁻¹ is observed compared to the spectrum of pure Krytox™. This is due to the global decrease of the number of CF_x groups as the perfluoropoly(ether) Krytox™ is replaced by the much shorter PFDTs molecule. However, the lower but still present band (a) observed in spectrum (E) indicates that Krytox™ is still not completely removed even after several washing steps.

XPS

In order to prove the successful grafting of PFDTs onto MNPs, samples were also analysed by XPS. Fig. 8 and 9 present the evolution of XPS spectra of C_{1s} and O_{1s} sub-regions of the Krytox™-surfacted and PFDTs-silanized ferrofluids

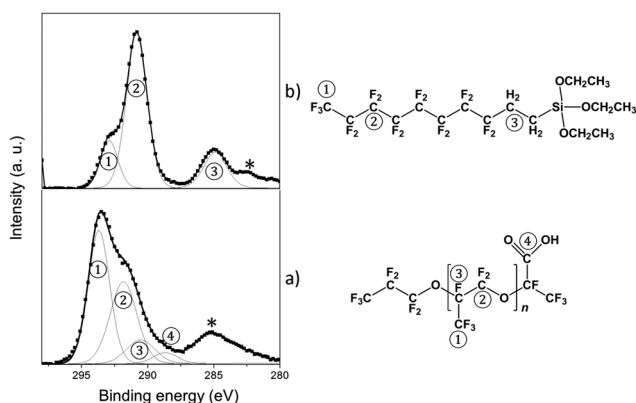


Fig. 8 De-convoluted XPS spectra in the C_{1s} region for (a) the Krytox™-surfacted ferrofluid, and (b) the PFDTs-silanized ferrofluid. Peaks noted with (*) are artefacts ascribed to satellites of the non-monochromatic source of X-rays. The formulae represent molecules before reaction.

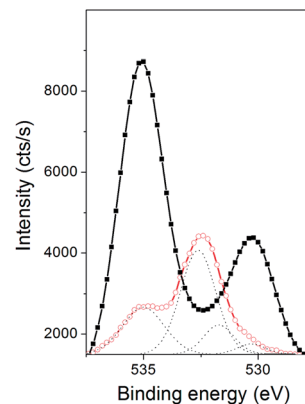


Fig. 9 XPS spectra in the O_{1s} region for Krytox™-surfacted ferrofluid (black line), PFDTs-silanized ferrofluid (red line) and deconvolution of XPS spectrum of PFDTs-silanized ferrofluid (dotted line).

Table 2 Surface elemental concentration obtained by XPS

Surface elemental concentration (%)	Si _{2p}	O _{1s}	C _{1s}	F _{1s}	Fe _{3p}
γ-Fe ₂ O ₃ control ^a	2.06	51	27.19	4.34	15.4
Surfacted-ferrofluid	0.31	11.16	27.57	59.19	1.77
Silanized-ferrofluid	3.2	6.22	29.01	61.24	0.33
PFDTs powder ^b	4.19	6.35	30.24	59.22	0

^a Possibly contaminated by PFDTs. ^b After hydrolysis–condensation.

respectively. The corresponding surface elemental concentrations are presented in Table 2.

In the C_{1s} region (Fig. 8a), the de-convoluted XPS spectrum of the Krytox™-surfacted ferrofluid presents three peaks (1, 2, 3) at 294, 292 and 291 eV attributed respectively to carbon in CF₃, CF₂ and CF groups of Krytox™. The peak (4) at 288 eV is assigned to carbon of carboxylate groups. After grafting of PFDTs onto the MNPs (Fig. 8b), a new peak at 285 eV reveals the presence of carbon in alkyl chains of PFDTs,⁵⁰ such CH₂ groups being absent in the Krytox™ perfluoropoly(ether). The strong decrease of the intensity of the peak at 294 eV indicates that Krytox™ is almost entirely eliminated.

In the O_{1s} region (Fig. 9), the XPS spectrum of the Krytox™-surfacted ferrofluid exhibits two peaks at 530.2 eV and 535.1 eV attributed respectively to oxygen in the γ-Fe₂O₃ environment and in perfluoropropylene oxide groups of Krytox™. The deconvoluted XPS-spectrum of the O_{1s} region of the 'silanized' ferrofluid shows that after grafting, the O_{1s} peak corresponding to oxygen from maghemite practically disappears in favour of a new peak at 532 eV. This peak at +2 eV is generally attributed to the formation of Si–O bonds and the peak at 531.2 eV, obtained after deconvolution, is assigned to the formation of Fe–O–Si bonds.⁵¹ The strong intensity decrease of the peak at 535 eV, assigned to the oxygen in the perfluoropoly(ether) chains, indicates that Krytox™ is almost entirely eliminated during the washing steps. The disappearance of the peak at 530 eV after silanization is correlated with a silica coating around the MNPs. Moreover, the concentration of

iron atoms on the surface of MNPs (Table 2) decreases strongly from 1.7 to 0.4 after grafting whereas the concentration of Si reaches 3%. The elemental concentrations measured for the silanized-ferrofluid are extremely close to those calculated for the pure PFDTS powder. These observations are consistent with the formation of a dense silica shell, which attenuates the photoelectrons and almost totally hides the iron atoms at the surface of the MNPs.

The XPS and FT-IR spectroscopy results are thus in total agreement with evidence the success of the chemical grafting reaction of fluoroalkylsilane onto the iron oxide surface.

Magnetic properties of the suspensions in fluorinated oils

The magnetisation curves of PFDTS-silanized MNPs (sample 1, LP) were obtained from superconducting quantum interference device (SQUID) magnetometry measurements at 300 K (Fig. 10). After subtracting the diamagnetic contribution of the solvent, the magnetisation curve $M(H)$ follows a Langevin law describing

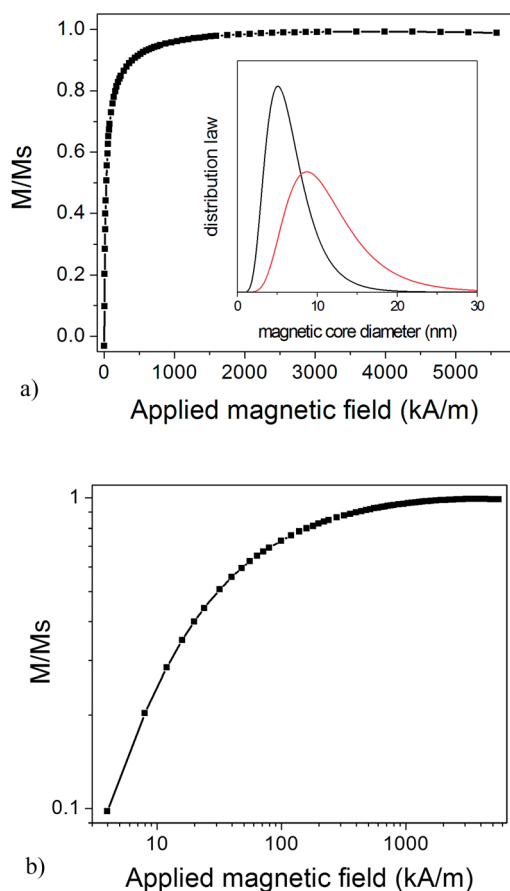


Fig. 10 (a) Magnetisation curve of the PFDTS-silanized ferrofluid sample 1 (LP) in FC-75 ($\phi = 1\%$ v/v) using the SQUID normalised by the saturation value at high field; inset: log-normal distribution of magnetic inorganic core diameters: by number (black line) and by volume (red line); (b) magnetisation curve on a log–log plot to highlight the fit quality at low field. The value of saturation magnetisation (plateau value) is $M_s = \phi m_{\text{spe}}$ where the value of specific magnetisation is $m_{\text{spe}} = 3 \times 10^5 \text{ A m}^{-1}$ (300 emu cm^{-3} in CGS units) and $\phi = 1\%$ is the volume fraction of iron oxide in the suspension.

the progressive orientation of the magnetic moments along the magnetic field followed by their saturation at a plateau value M_s . This saturation magnetisation reads $M_s = \phi m_{\text{spe}}$, where m_{spe} is the specific magnetisation approximately equal to $3 \times 10^5 \text{ A m}^{-1}$ for colloidal maghemite nanoparticles and ϕ is the MNP volume fraction (the magnetisation being defined as the volume density of magnetic moments).³⁵ This superparamagnetic behaviour in the liquid state direct evidences that the silanization reaction at the surface of the MNPs enabled their stabilisation against aggregation up to a magnetic field induction as high as 7 T.

The magnetic susceptibility defined as the slope of the magnetisation curve at low field was $\chi = 0.05$ for this sample diluted at $\phi = 1\%$. Therefore, the susceptibility of samples at any volume fraction can be calculated by $\chi = 5\phi$. The exact shape of the measured magnetisation curve $M(H)$ could be fitted by the convolution of the Langevin law of superparamagnetism with a size distribution of the MNPs for which we assume a log-normal law^{35,52} as written in eqn (1). By this method, we obtained a median diameter $d_0^{\text{SQUID}} = 6.1 \text{ nm}$ and a logarithmic size width $\sigma^{\text{SQUID}} = 0.42$. The inset of Fig. 10a shows the particle size distribution by number and by volume. The number-averaged diameter $d_n^{\text{SQUID}} = 6.7 \text{ nm}$ is determined by eqn (2), whereas the volume-averaged diameter $d_w^{\text{SQUID}} = 11.4 \text{ nm}$ is calculated by eqn (3). These two values are both smaller than those obtained by TEM image analysis ($d_n^{\text{TEM}} = 10.2 \text{ nm}$ and $d_w^{\text{TEM}} = 19.1 \text{ nm}$). This difference is ascribed to the reported presence of a nonmagnetic dead layer around ferrite MNPs^{53–55} and to the silicon-rich shell that is visible in the TEM images but does not contribute to the magnetic properties.

Preparation of monodisperse magnetic emulsions as medium for acoustic measurements

To evidence great potential applications of silanized fluorinated ferrofluids to control the propagation of ultrasounds, we prepared narrowly size-dispersed emulsions in a water-based Carbopol™ yield-stress matrix, whose interest is to oppose to the settlement of droplets by gravity (fluorinated oils being much denser than aqueous media). We show here the results obtained with an emulsion prepared with the LP ‘silanized’ ferrofluid (sample 1) composed of MNPs with a hydrodynamic diameter of 51 nm (PDI = 0.05). TEM micrographs of ‘silanized’ sample 1 showed magnetic core sizes of $9.3 \pm 3.4 \text{ nm}$. A volume fraction of maghemite $\phi = 6\%$ in the ferrofluid was determined using UV-spectroscopy and mass density measurement. To check the ability of the ferrofluid droplets to be deformed by a magnetic field, droplets of diameter around $200 \mu\text{m}$ were suspended in the Carbopol™ gel at 0.05% w/w.

Response of a single droplet to an applied magnetic field

The droplet elongation under a magnetic field is characterised by its aspect ratio a/b , where a and b are respectively the long and short axes of the ellipsoidal shape, measured as a function of the applied induction B . From Fig. 11a, it appears that the aspect ratio can reach up to 2.5 for an external field induction B of 45 mT.

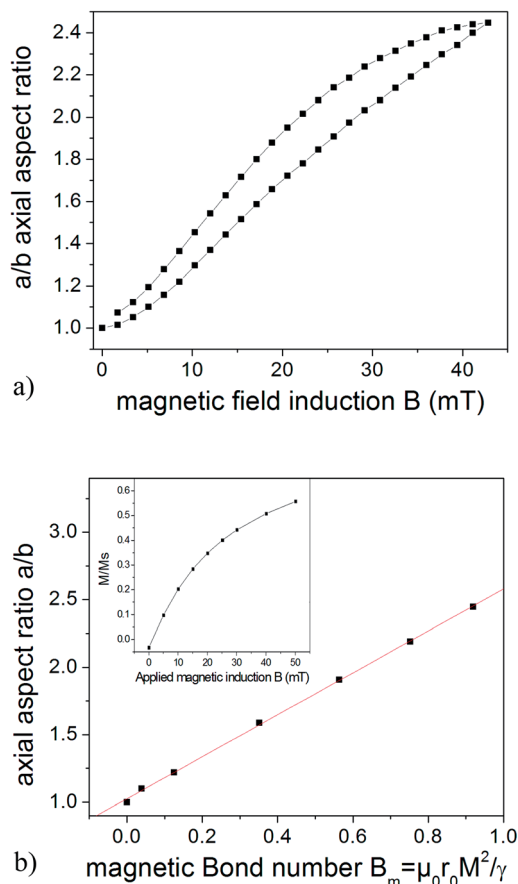


Fig. 11 (a) Evolution of the axial aspect ratio a/b of a droplet of the PFDTs-silanized ferrofluid suspended in a water-based gel, of initial radius $r_0 = 104 \mu\text{m}$, under increasing values of magnetic induction B . The apparent hysteresis when the field is decreased back to zero is ascribed to slow relaxation of the gel medium (typically 30 s) when the magnetic pressure is released; (b) variation of the axial aspect ratio a/b of the fluorinated ferrofluid droplet represented as a function of the magnetic Bond number B_m , defined as 4 times the ratio of the magnetic pressure acting on the interface at the two poles by the Laplace pressure of the initially spherical droplet. The linear fit (slope $\pi/2$, intercept 1) is a theoretical prediction at low deformation.⁵⁶ Inset: enlargement at low field of the reduced magnetization relatively to the saturation M/M_s vs. induction B . This reduced plot of the SQUID data measured at a $\phi = 1\%$ enables calculation of the magnetization at any volume fraction ϕ of the same magnetic nanoparticles, in particular the emulsion droplet in the gel using the calculated saturation magnetization $M_s = \phi m_{\text{spe}}$ with $m_{\text{spe}} = 3 \times 10^5 \text{ A m}^{-1}$, e.g. $M_s = 1.8 \times 10^4 \text{ A m}^{-1}$ for $\phi = 6\%$.

The deformation of an isolated ferrofluid droplet by a magnetic field was studied several decades ago both theoretically⁵⁶ and experimentally.⁵⁷ The model is very robust and has been verified by experimental studies on aqueous biphasic ferrofluids^{58,59} and on non aqueous, e.g. silicone,⁶⁰ ferrofluid droplets. Fig. 11b shows another representation of the axial aspect ratio a/b of the ferrofluid droplet as a function of the magnetic Bond number B_m . This adimensional number compares the magnetic pressure P_m acting on the interface between the ferrofluid droplet and the non-magnetic gel to the Laplace pressure ΔP_L arising from the curvature of the initial droplet:

$$B_m = 4 \frac{P_m}{\Delta P_L} = \frac{\mu_0 r_0 M^2}{\gamma} \quad (4)$$

where $\mu_0 = 4\pi \times 10^{-7} \text{ kg m A}^{-2} \text{ s}^{-2}$ is the magnetic permeability of vacuum, γ is the interfacial tension between the ferrofluid and the surrounding fluid (here the aqueous yield-stress gel), and the values of magnetisation M were obtained from the SQUID measurement curve M/M_s vs. B at low field (inset of Fig. 11b) with $M_s = \phi m_{\text{spe}}$ where $\phi = 6\%$ and $m_{\text{spe}} = 3 \times 10^5 \text{ A m}^{-1}$.

The droplet radius $r_0 = (3V/4\pi)^{1/3}$ is measured at $104 \mu\text{m}$ from the volume V that remained constant within 1% when plotting $V = 4\pi ab^2/3$ whatever the applied field strength (data not shown). The values of B_m were calculated using M values corresponding to each magnetic field applied to elongate the droplet of the PFDTs-silanized ferrofluid. We observed that the axial aspect ratio a/b varies perfectly linearly with B_m . Such linearity is generally observed at low B_m values, typically for aspect ratios below 3.⁵⁷ Introducing a theory of the deformation of magnetic droplets at any B_m values, Tsebers⁵⁶ showed that at low deformation, when the eccentricity of the ellipsoidal shape, defined by $e = \sqrt{1 - b^2/a^2}$, tends towards zero, then the magnetic Bond number varies as:

$$B_m \approx e^2/\pi \quad (5)$$

when $e \rightarrow 0$, one approximates $a/b = (1 - e^2)^{-0.5} \approx 1 + 0.5e^2$, thus we deduce the equation giving the aspect ratio variation in the linear regime:

$$a/b \approx 1 + \frac{\pi}{2} B_m \quad (6)$$

By fitting the experimental plot of a/b vs. B_m with a line of slope $\pi/2$ and intercept 1, we obtain the value $\gamma = 11.8 \text{ mN m}^{-1}$ for the interfacial tension, in excellent agreement with the interfacial tension $\gamma = 11 \text{ mN m}^{-1}$ measured by the pendant drop method. The Laplace pressure difference $\Delta P_L = 2\gamma/r_0$ between the interior of the initially spherical droplet and the gel is estimated at $\Delta P_L = 230 \text{ Pa}$ with the interfacial tension deduced previously. Therefore, even if the applied field is at its lowest value corresponding to $B_m = 0.04$, the pressure acting on the magnetic poles of the droplet is estimated at $P_m \approx 0.01 \times 230 = 2.3 \text{ Pa}$. This value is slightly above the yield stress of the gel (measured value of 1.5 Pa). We can thus conclude that the applied magnetic pressure overcomes the yield stress of the water-based gel, which allows fluid motion around the droplet accompanying its deformation. In the opposite situation when the droplet is elongated and the magnetic field is switched off, the slow shape relaxation kinetics can be ascribed to a pressure gap between the poles and the equator of the ellipsoid lower than P_m acting when the field was on, but still sufficient to cause the flow of the gel (*i.e.* above the yield stress).

Monodisperse magnetic emulsions in the water-based gel

The silanized fluorinated ferrofluid was injected through a silica capillary (with an internal diameter ID of 40 or $75 \mu\text{m}$) into the gel (Carbopol™ $0.05\% \text{ w/w}$) under a controlled pressure.^{14,38}

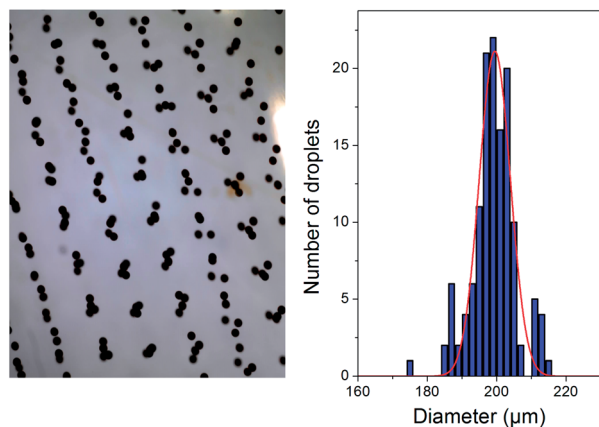


Fig. 12 Optical micrograph and the corresponding size histogram deduced from image analysis of a magnetic fluorinated emulsion. Volume fraction $\approx 0.5\%$ of the matrix (0.05% w/w CarbopolTM). Droplets containing $\phi = 6\%$ v/v of MNPs ('silanized' sample 1) were deposited through a capillary of ID = 40 μm under a 1.7 bar air pressure, translated at a speed of 1 mm s^{-1} . The distribution yielded an average diameter of 199 μm with $\text{CV} = 3.2\%$ (measured on 133 droplets).

The deposition was obtained by motorised translation of the plate at a speed of 1 mm s^{-1} (Fig. 12) for the smaller capillary or 10 mm s^{-1} for the larger one. The yield stress of the CarbopolTM gel was measured at 1.5 Pa for a concentration of 0.05% w/w by standard rheological measurement (cone-plan AR2000 rheometer). We calculated that fluorinated ferrofluid droplets (mass density $d = 1.9 \text{ g cm}^{-3}$) can stay suspended as long as their diameter remains lower than 250 μm (balancing the hydrostatic pressure $P_h = 2/3r_0g\rho$ with the yield stress). The sizes of the emulsion droplets were measured on optical images. The mean diameter and coefficient of variation CV (ratio of the standard width to the mean value, assuming Gaussian distribution) were deduced from these measurements on a large statistics. The conclusion is that nearly monodisperse magnetic emulsions can be produced by this method, an example being presented in Fig. 12.

Acoustic properties

These emulsions were analysed by multiple-echo ultrasound spectroscopy acquired with a piezoelectric transducer of 5 MHz central frequency stuck directly on the measurement cell. Fig. 13 shows the evolution of the attenuation coefficient *vs.* frequency curves for magnetic inductions of 0, 20, and 40 mT. Under a zero magnetic field, the attenuation spectrum exhibits several peaks at specific frequencies, in accordance with previous results obtained for pure (non magnetic) fluorocarbon emulsions of $\text{CV} \approx 5\%$.³⁸ These attenuation peaks result from Mie resonances created by the sound-speed contrast existing between the host matrix and the fluorinated ferrofluid droplets.

When a magnetic field was applied perpendicularly to the direction of acoustic wave propagation, these attenuation peaks were shifted towards higher frequencies. This evolution is explained by the shape change of the ferrofluid droplets from spheres to ellipsoids, in that case elongated perpendicularly to

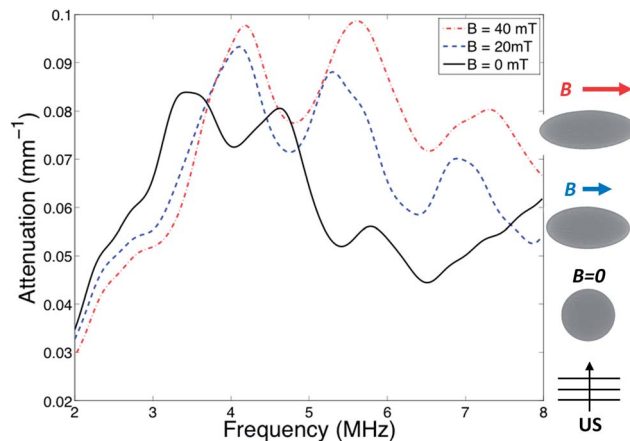


Fig. 13 Acoustic spectrum (attenuation coefficient *vs.* wave frequency) for increasing magnetic field induction values B (mT) applied perpendicularly to the propagation direction of the ultrasound wave.

the US wave propagation vector. Qualitatively, the dimension of the droplets probed by ultrasound becomes smaller, thus the resonance frequencies become higher. A quantitative description of this effect with a complete fitting of the spectra under varying magnetic field strengths and directions is the subject of another article.¹⁵

4 Conclusions

In summary, we described a chemical route based on aqueous coprecipitation synthesis, perfluoropoly(ether) surfactant coating, ligand exchange and sol-gel reaction to achieve a stable fluorinated ferrofluid. After silanization, the MNPs coated by a thin fluorinated silica shell can be dispersed individually in any fluorinated oil. The obtained dispersions of silanized-MNPs exhibiting a high colloidal stability and low viscosity were used to prepare monodisperse emulsions in a water-based Bingham gel with a microfluidic injection device. The lower viscosity compared to a mere 'surfacted' ferrofluid is ascribed to the replacement of the macromolecular surfactant with a thin layer of much shorter perfluorosilane (since in the denomination KrytoxTM 157-FSH, the H letter means "high viscosity"). Concerning the decrease of interfacial tension γ with the aqueous phase, this might be a consequence of the ligand-exchange that causes desorption of the surfactant from the iron oxide surface and adsorption of a small fraction of KrytoxTM still remaining after the washing steps (as seen by FT-IR spectroscopy and XPS) at the fluorinated oil/water interface. Such a reducing effect of γ was indeed also noticed with another fluorinated surfactant, Dupont ZonylTM FSO (data not shown).

The droplet shape elongates along the direction of the applied magnetic field. These reversible deformations can be perfectly controlled by modulating the magnetic field induction. Acoustic measurements have shown that these emulsions behave as "resonant materials" exhibiting attenuation peaks at specific frequencies in the Mie scattering regime. By applying a magnetic field, we can tune the resonant acoustic response of

such a scattering medium in a reversible manner. By varying the magnetic field from 0 to 40 mT, we can precisely control the attenuation frequency and the attenuation coefficient of the material. The droplets described here have a radius around 100 μm , while typical diameters of “microbubbles” used as contrast agents in ultra-sonography are rather in the 1–10 μm range, *i.e.* not larger than those of red blood cells, to avoid clogging of blood vessels or kidney. Nevertheless, magnetic emulsions allow a convenient size selection using a method based on their sensitivity to an external magnetic field, by forming dipolar chains preferably made of droplets of analogous diameter, and that can be separated by a field strength gradient.^{61,62} Starting from a polydisperse magnetic emulsion, this size-grading method can lead to monodisperse emulsions with target sizes ranging from the sub-micrometric up to the millimetric range, thus opening the way to acoustic applications from the audible (20 Hz to 20 kHz) to the US regime (100 kHz to 10 MHz). The locally resonant emulsions described in this article appear to be the constitutive brick elements for the preparation of tuneable acoustic materials.⁶³

Abbreviations

ATR	Attenuated total reflection
CV	Coefficient of variation
DLS	Dynamic light scattering
FT-IR	Fourier transform infrared spectroscopy
ID	Internal diameter
LP	Large particles
MNP	Magnetic nanoparticle
OD	Outer diameter
PDI	Polydispersity index
PFDTS	Perfluorodecyltriethoxysilane
PFOA	Perfluorooctanoic acid
PFOB	Perfluorooctylbromide
SANS	Small angle neutron scattering
SLD	Scattering length density
SP	Small particles
SQUID	Superconducting quantum interference device
TEM	Transmission electron microscopy
TMAOH	Tetramethylammonium hydroxide
UCA	Ultrasound contrast agents
US	Ultrasound
XPS	X-ray photoelectron spectroscopy.

Acknowledgements

This work was supported by the US Air Force European Office of Aerospace Research and Development (EOARD Grants FA8655-11-M-4006 and FA8655-12-1-2067), by the Agence Nationale de la Recherche (ANR Grant 2011-BS0902101), and by the Conseil Régional d'Aquitaine and the Polytechnic Institute of Bordeaux. We thank Rodolphe Clérac and Mathieu Rouziers at CRPP (UPR8641 CNRS/Université de Bordeaux) for the SQUID curves and Christine Labrugère at ICMCB (UPR9048 CNRS/Université de Bordeaux) for the XPS spectra.

Notes and references

- R. Berger, G. Resnati, P. Metrangolo, E. Weber and J. Hulliger, *Chem. Soc. Rev.*, 2011, **40**, 3496–3508.
- R. C. Buck, J. Franklin, U. Berger, J. M. Conder, I. T. Cousins, P. de Voogt, A. A. Jensen, K. Kannan, S. A. Mabury and S. P. J. van Leeuwen, *Integr. Environ. Assess. Manage.*, 2011, **7**, 513–541.
- N. Kudo and Y. Kawashima, *J. Toxicol. Sci.*, 2003, **28**, 49–57.
- A. B. Lindstrom, M. J. Strynar and E. L. Libelo, *Environ. Sci. Technol.*, 2011, **45**, 7954–7961.
- E. G. Schutt, D. H. Klein, R. M. Mattrey and J. G. Riess, *Angew. Chem., Int. Ed.*, 2003, **42**, 3218–3235.
- E. Stride and M. Edirisinghe, *Soft Matter*, 2008, **4**, 2350–2359.
- O. Diou, N. Tsapis, C. I. Giraudeau, J. Valette, C. Gueutin, F. Bourasset, S. Zanna, C. Vauthier and E. Fattal, *Biomaterials*, 2012, **33**, 5593–5602.
- S. Rossi, G. Waton and M. P. Krafft, *Langmuir*, 2009, **26**, 1649–1655.
- S. Rossi, C. Szijjarto, F. Gerber, G. Waton and M.-P. Krafft, *J. Fluorine Chem.*, 2011, **132**, 1102–1109.
- D. Vlaskou, O. Mykhaylyk, F. Krötz, N. Hellwig, R. Renner, U. Schillinger, B. Gleich, A. Heidsieck, G. Schmitz, K. Hensel and C. Plank, *Adv. Funct. Mater.*, 2010, **20**, 3881–3894.
- A. L. Klivanov, T. I. Shevchenko, B. I. Raju, R. Seip and C. T. Chin, *J. Controlled Release*, 2010, **148**, 13–17.
- J. Owen, B. Zhou, P. Rademeyer, M.-X. Tang, Q. Pankhurst, R. Eckersley and E. Stride, *Theranostics*, 2012, **2**, 1127–1139.
- P. N. Nguyen, G. Nikolova, P. Polavarapu, G. Waton, L. T. Phuoc, G. Pourroy and M. P. Krafft, *RSC Adv.*, 2013, **3**, 7743–7746.
- T. Brunet, S. Raffy, B. Mascaro, J. Leng, R. Wunenburger, O. Mondain-Monval, O. Poncelet and C. Aristégui, *Appl. Phys. Lett.*, 2012, **101**, 011913.
- T. Brunet, K. Zimny, B. Mascaro, O. Sandre, O. Poncelet, C. Aristégui and O. Mondain-Monval, *Phys. Rev. Lett.*, 2013, **111**, 264301.
- H.-C. Zhou, J. R. Long and O. M. Yaghi, *Chem. Rev.*, 2012, **112**, 673–674.
- C. B. Kristalyn, S. Watt, S. A. Spanninga, R. A. Barnard, K. Nguyen and Z. Chen, *J. Colloid Interface Sci.*, 2011, **353**, 322–330.
- K. Tsujii, T. Yamamoto, T. Onda and S. Shibuichi, *Angew. Chem., Int. Ed. Engl.*, 1997, **36**, 1011–1012.
- Z. Xu, Q. Liu and J. A. Finch, *Appl. Surf. Sci.*, 1997, **120**, 269–278.
- M. Yamaura, R. L. Camilo, L. C. Sampaio, M. A. Macêdo, M. Nakamura and H. E. Toma, *J. Magn. Magn. Mater.*, 2004, **279**, 210–217.
- A. del Campo, T. Sen, J.-P. Lellouche and I. J. Bruce, *J. Magn. Magn. Mater.*, 2005, **293**, 33–40.
- S. Mornet, J. Portier and E. Duguet, *J. Magn. Magn. Mater.*, 2005, **293**, 127–134.
- I. J. Bruce and T. Sen, *Langmuir*, 2005, **21**, 7029–7035.
- W. Wu, Q. He and C. Jiang, *Nanoscale Res. Lett.*, 2008, **3**, 397–415.

- 25 F. Galeotti, F. Bertini, G. Scavia and A. Bolognesi, *J. Colloid Interface Sci.*, 2011, **360**, 540–547.
- 26 N. Arsalani, H. Fattahi, S. Laurent, C. Burtea, L. V. Elst and R. N. Muller, *Contrast Media Mol. Imaging*, 2012, **7**, 185–194.
- 27 T. Borase, T. Ninjbadgar, A. Kapetanakis, S. Roche, R. O'Connor, C. Kerskens, A. Heise and D. F. Brougham, *Angew. Chem., Int. Ed.*, 2013, **52**, 3164–3167.
- 28 R. De Palma, S. Peeters, M. J. Van Bael, H. Van den Rul, K. Bonroy, W. Laureyn, J. Mullens, G. Borghs and G. Maes, *Chem. Mater.*, 2007, **19**, 1821–1831.
- 29 J. Trekker, K. Jans, H. Damm, D. Mertens, T. Nuytten, J. Vanacken, V. Moshchalkov, J. D'Haen, T. Stakenborg, W. Van Roy, U. Himmelreich and L. Lagae, *Magnetics, IEEE Transactions on*, 2013, **49**, 219–226.
- 30 N. Kohler, G. E. Fryxell and M. Zhang, *J. Am. Chem. Soc.*, 2004, **126**, 7206–7211.
- 31 T. Ninjbadgar and D. F. Brougham, *Adv. Funct. Mater.*, 2011, **21**, 4769–4775.
- 32 D. Forge, S. Laurent, Y. Gossuin, A. Roch, L. Vander Elst and R. N. Muller, *J. Magn. Magn. Mater.*, 2011, **323**, 410–415.
- 33 Y. Sun, X. Ding, Z. Zheng, X. Cheng, X. Hu and Y. Peng, *Eur. Polym. J.*, 2007, **43**, 762–772.
- 34 R. Massart, *Magnetics, IEEE Transactions on*, 1981, **17**, 1247–1248.
- 35 R. Massart, E. Dubois, V. Cabuil and E. Hasmonay, *J. Magn. Magn. Mater.*, 1995, **149**, 1–5.
- 36 K. L. O'Neal, H. Zhang, Y. Yang, L. Hong, D. Lu and S. G. Weber, *J. Chromatogr. A*, 2010, **1217**, 2287–2295.
- 37 V. Leroy, A. Strybulevych, J. H. Page and M. G. Scanlon, *J. Acoust. Soc. Am.*, 2008, **123**, 1931–1940.
- 38 B. Mascaro, T. Brunet, O. Poncelet, C. Aristégui, S. Raffy, O. Mondain-Monval and J. Leng, *J. Acoust. Soc. Am.*, 2013, **133**, 1996–2003.
- 39 M. Safi, H. Sarrouj, O. Sandre, N. Mignet and J.-F. Berret, *Nanotechnology*, 2010, **21**, 145103.
- 40 P. Arosio, J. Thévenot, T. Orlando, F. Orsini, M. Corti, M. Mariani, L. Bordonali, C. Innocenti, C. Sangregorio, H. Oliveira, S. Lecommandoux, A. Lascialfari and O. Sandre, *J. Mater. Chem. B*, 2013, **1**, 5317–5328.
- 41 A. Brulet, D. Lairez, A. Lapp and J.-P. Cotton, *J. Appl. Crystallogr.*, 2007, **40**, 165–177.
- 42 I. P. Vinogradov, A. Dinkelmann and A. Lunk, *Surf. Coat. Technol.*, 2003, **174–175**, 509–514.
- 43 L. Zhang, R. He and H.-C. Gu, *Appl. Surf. Sci.*, 2006, **253**, 2611–2617.
- 44 Y. Ren, K.-i. Iimura and T. Kato, *Langmuir*, 2001, **17**, 2688–2693.
- 45 N. Wu, L. Fu, M. Su, M. Aslam, K. C. Wong and V. P. Dravid, *Nano Lett.*, 2004, **4**, 383–386.
- 46 A. L. Willis, N. J. Turro and S. O'Brien, *Chem. Mater.*, 2005, **17**, 5970–5975.
- 47 A. Vilcnik, I. Jerman, A. Surca Vuk, M. Kozelj, B. Orel, B. Tomsic, B. Simoncic and J. Kovac, *Langmuir*, 2009, **25**, 5869–5880.
- 48 T. J. Lenk, V. M. Hallmark, C. L. Hoffmann, J. F. Rabolt, D. G. Castner, C. Erdelen and H. Ringsdorf, *Langmuir*, 1994, **10**, 4610–4617.
- 49 J. L. Blin and C. Carteret, *J. Phys. Chem. C*, 2007, **111**, 14380–14388.
- 50 A. Chandekar, S. K. Sengupta and J. E. Whitten, *Appl. Surf. Sci.*, 2010, **256**, 2742–2749.
- 51 M. R. Turner, E. Duguet and C. Labrugère, *Surf. Interface Anal.*, 1997, **25**, 917–923.
- 52 R. W. Chantrell, J. Popplewell and S. Charles, *Magnetics, IEEE Transactions on*, 1978, **14**, 975–977.
- 53 K. Haneda and A. H. Morrish, *Magnetics, IEEE Transactions on*, 1980, **16**, 50–52.
- 54 Y.-w. Jun, J.-w. Seo and J. Cheon, *Acc. Chem. Res.*, 2008, **41**, 179–189.
- 55 M. P. Morales, S. Veintemillas-Verdaguer, M. I. Montero, C. J. Serna, A. Roig, L. Casas, B. Martínez and F. Sandiumenge, *Chem. Mater.*, 1999, **11**, 3058–3064.
- 56 A. O. Tsebers, *Magneto hydrodynamics*, 1985, **21**, 19–26.
- 57 V. I. Arkhipenko, Y. D. Barkov and V. G. Bashstovoi, *Magneto hydrodynamics*, 1978, **14**, 373–375.
- 58 J. C. Bacri and D. Salin, *J. Phys., Lett.*, 1982, **43**, 649–654.
- 59 O. Sandre, J. Browaeys, R. Perzynski, J. C. Bacri, V. Cabuil and R. E. Rosensweig, *Phys. Rev. E: Stat. Phys., Plasmas, Fluids, Relat. Interdiscip. Top.*, 1999, **59**, 1736–1746.
- 60 S. Afkami, A. J. Tyler, Y. Renardy, M. Renardy, T. G. St. Pierre, R. C. Woodward and J. S. Riffle, *J. Fluid Mech.*, 2010, **663**, 358–384.
- 61 J. Bibette, *J. Magn. Magn. Mater.*, 1993, **122**, 37–41.
- 62 F. Montagne, O. Mondain-Monval, C. Pichot, H. Mozzanega and A. Elaissari, *J. Magn. Magn. Mater.*, 2002, **250**, 302–312.
- 63 T. Brunet, J. Leng and O. Mondain-Monval, *Science*, 2013, **342**, 323–324.